Available online at www.sciencedirect.com

ScienceDirect

Procedia Manufacturing 47 (2020) 1170–1177

Procedia MANUFACTURING

www.elsevier.com/locate/procedia

23rd International Conference on Material Forming (ESAFORM 2020)

Numerical Analysis of Residual Stresses in Parts Produced by Selective Laser Melting Process

Bruno M. Marques[a], Carlos M. Andrade[a], Diogo M. Neto[a,*], Marta C. Oliveira[a], José L. Alves[b] and Luís F. Menezes[a]

[a]*CEMMPRE, Department of Mechanical Engineering, University of Coimbra, Rua Luís Reis Santos, Pinhal de Marrocos, 3030-788 Coimbra, Portugal*
[b]*CMEMS, Microelectromechanical Systems Research Unit, University of Minho, Campus de Azurém, 4800-058 Guimarães, Portugal*

* Corresponding author. Tel.: +351-239-790-700; fax: +351-239-790-701. *E-mail address:* diogo.neto@dem.uc.pt

Abstract

Additive manufacturing (AM) of metallic components has received large attention in the last decade, particularly the selective laser melting (SLM) process, due to its ability to produce complex and customized parts. However, the high residual stresses generated by the thermal cycles can lead to significant distortions and ultimately to the part cracking. Therefore, several numerical simulation tools have been adopted to predict and mitigate the unwanted part distortion. This study presents a thermo-mechanical model able to simulate the SLM process, considering multi-track within a single powder layer. The finite element model considers the powder-liquid-solid phase changes, i.e. includes melting, solidification and cooling phenomena. The thermal analysis is based on the transient heat conduction problem, considering a volumetric moving heat source. The mechanical analysis is based in an elastoplastic constitutive law, which predicts the residual stresses through the strains induced by the thermal gradients. Both the thermal and the mechanical material properties are assumed as temperature dependent. The main goal of this study is to assess the effect of the scan strategy on the residual stresses generated in the built component. In this context, unidirectional and alternating scan strategies are compared in terms of thermal history and consequent residual stresses generated.

Keywords: Additive manufacturing; Selective laser melting; Thermo-mechanical modeling; Residual stresses

1. Introduction

Additive manufacturing (AM) processes have received an increasing attention in the last decade, particularly the metal powder based technologies, which have been applied to produce highly-customized metallic components [1]. Selective Laser Melting (SLM) is a category of AM processes, in which parts are built layer-by-layer using the laser beam energy to melt predefined regions of each thin layer of powder. The moving heat source leads to heating, melting and solidification of the metallic alloy, creating repeated heating and cooling conditions on the work piece [2]. Accordingly, this process has a great potential to produce complex parts with high-performance designs, including the eventual pointwise control of microstructure and mechanical properties [3].

However, the large temperature gradients generated during the SLM process result in the formation of high residual stresses in the finished part, whose magnitude can exceed the yield strength of the alloy [4]. Thus, these resulting residual stresses may have a detrimental influence on dimensional accuracy (thin-walled features) and mechanical performance [5]. Among the several process parameters, the laser scan strategy is known to affect significantly the residual stress fields [6], as well as the final microstructure of parts fabricated by SLM [7]. Indeed, one of the principal challenges of AM processes is the actual incapability to predict the mechanical properties of the final parts.

10.1016/j.promfg.2020.04.167

The numerical simulation can provide a better understanding of the SLM process, a better predictability of the part properties and create guidelines for the optimization of the manufacturing process. Nevertheless, the multi-physics and multi-scale nature of this AM process represents a big challenge for numerical simulation tools. Several computational tools have been recently developed, using macro-scale [8], meso-scale [9] and multi-scale modeling [10]. The interaction between thermal and mechanical responses demands the development of reliable thermo-mechanical coupling models for the residual stress analysis in the SLM process. Therefore, the accurate prediction of the residual stresses and the unwanted part distortions requires an accurate temperature field estimation.

The complex physical phenomena associated with the melt pool are mainly controlled by mass and heat transfer [11]. The main heat transfer mechanism within the melt pool is the convective, which is driven by gravity, buoyancy, surface tension, capillarity and Marangoni effects [12]. Thus, micro-scale models have been used in the melt pool dynamics, comprising the interaction between the laser beam and the powder particles, heat transfer, phase change, capillary and Marangoni forces, evaporation pressure and wetting [13]. However, the computational cost tends to be very high, particularly when more effects are included and the entire thermal history is required [14].

Since an effective analysis of the SLM process requires the adoption of macro-scale models, the finite element method is typically used to predict the transient temperature distribution in the parts obtained by SLM. Then, using obtained temperature field, the thermal stress field and the residual stresses can be estimated by a thermo-mechanical coupling model [15]. However, this process involves large temperature changes, which leads to strong variations of the thermo-mechanical properties and consequently generates a nonlinear problem. Although the SLM process is inherently multi-layer, most of the studies are focused on single layer deposition [16]. This simplification allows to reduce significantly the computational cost but neglects the thermal exchanges between successive layers, affecting the predicted stress field.

The main goal of this study is to assess the effect of the laser scan strategy on the residual stresses generated in the production of a Ti-6Al-4V component, considering a multi-track SLM process in a single layer. The proposed model predicts the evolution of temperature and thermal stress fields, and the residual stresses of the printed part.

2. Thermo-mechanical model

In the present study, the numerical analysis of the SLM process is carried out using a 3D thermo-mechanical modelling approach, based on the staggered coupling proposed by Martins et al. [17]. This approach enables the evaluation of both the transient temperature and the mechanical stresses distribution, during the SLM process.

2.1. Heat transfer modeling

The differential equation governing the transient heat conduction, within a continuous medium with arbitrary volume, can be derived from the first law of thermodynamic. The solution of the heat equation provides the temperature T with respect to time t, expressed as follows:

$$k\left(\frac{\partial^2 T}{\partial x^2}+\frac{\partial^2 T}{\partial y^2}+\frac{\partial^2 T}{\partial z^2}\right)+\dot{q}=\rho c_{\mathrm{p}}\frac{\partial T}{\partial t}, \tag{1}$$

where k is the thermal conductivity coefficient, ρ denotes the mass density, c_{p} is the specific heat and $\dot{q}$ is the power generated per volume in the workpiece. In order to simplify the analysis, usually the specific heat is modified between the solidus and the liquidus temperatures to account for the latent heat, providing an apparent specific heat [18]. However, the latent heat was not considered in the model.

Due to the porosity in the powder bed, the incident laser radiation is reflected between the particles, increasing the absorption depth in comparison to the one observed for the bulk solid [19]. Thus, in order to describe the laser penetration into the powder bed, the laser heat input is modelled by the volumetric Gaussian heat source proposed by Goldak et al. [20]. The power density distribution for a hemispherical shape heat source model can be expressed as:

$$\dot{q}=\frac{2^{5/2}\beta P}{\pi^{3/2}{r_0}^3}\exp\left\{-2\frac{x^2+y^2+z^2}{{r_0}^2}\right\}, \tag{2}$$

where P is the power of the laser source, β is the absorptivity of the laser beam and r_0 denotes the radius of the laser beam. Nonetheless, it should be notice that in order to improve the accuracy of the numerical approximation of the melt pool geometry, more complex volumetric heat source models have been proposed [21].

Due to the preheating of the substrate, the initial temperature of the system (substrate and powder bed) is imposed (in this case 200ºC). Besides, the environment temperature is also known and assumed constant during the SLM process (set to 200ºC). The proposed model considers the heat loss by natural convection between the exposed powder bed surface and the environment. The heat exchange by convection to the environment on the top surface of the powder bed is determined by:

$$\dot{q}_{\mathrm{c}}=h_{\mathrm{c}}(T-T_{\infty}), \tag{3}$$

where h_{c} is the heat convection coefficient and T_{∞} is the environment temperature. The remaining surfaces (side walls and bottom surface) are assumed thermally isolated. The heat loss due to radiation was considered in the present model by increasing the heat convection coefficient [22], defined by h_{c} = 15 W/m^{2}K.

2.2. Mechanical modelling

In order to obtain the mechanical response of the workpiece during the manufacturing process, the *quasi*-static mechanical analysis is carried out using the current temperature field (obtained from the thermal analysis). The balance of linear

momentum in any point of the body (part to be manufactured) is given by:

$$\mathrm{div}(\boldsymbol{\sigma}) + \mathbf{b} = \mathbf{0}\,, \tag{4}$$

where $\boldsymbol{\sigma}$ is the stress tensor and $\mathbf{b}$ are the body forces, which are neglected in the present model. Regarding the boundary conditions, prescribed displacements are imposed on the Dirichlet boundary. In this study, the substrate bottom is fixed during SLM processing, including after cooling down.

The total strain increment is the superposition of the following terms:

$$\Delta\boldsymbol{\varepsilon}^{\mathrm{total}} = \Delta\boldsymbol{\varepsilon}^{\mathrm{e}} + \Delta\boldsymbol{\varepsilon}^{\mathrm{p}} + \Delta\boldsymbol{\varepsilon}^{\mathrm{th}}\,, \tag{5}$$

where $\Delta\boldsymbol{\varepsilon}^{\mathrm{e}}$ is the elastic strain increment, $\Delta\boldsymbol{\varepsilon}^{\mathrm{p}}$ is the plastic strain increment and $\Delta\boldsymbol{\varepsilon}^{\mathrm{th}}$ is the thermal strain increment. The effects of strains induced by solid-state phase transformation and creep are neglected in the present model.

The linear elastic constitutive law defines a linear relationship between the stress tensor and the strain tensor. Thus, the resulting stress from the elastic strain is expressed as:

$$\boldsymbol{\sigma}^{\mathrm{e}} = \mathbf{C} : \boldsymbol{\varepsilon}^{\mathrm{e}}\,, \tag{6}$$

where $\mathbf{C}$ is the fourth-order material stiffness tensor (Elastic moduli). Assuming an isotropic linear elastic material, the stiffness matrix $\mathbf{C}$ can be calculated from the Young's modulus (E) and the Poisson's ratio (ν).

Considering an associated flow rule in the plasticity model, the plastic strain increment is given by:

$$\Delta\boldsymbol{\varepsilon}^{\mathrm{p}} = \lambda \frac{\partial f}{\partial \boldsymbol{\sigma}}\,, \tag{7}$$

where λ is the plastic multiplier, which is calculated through the consistency condition. The plastic behavior is also assumed as isotropic, described by von Mises yield criteria. Hence the yield function f is obtained by:

$$f = \sigma_{\mathrm{vM}} - \sigma_{\mathrm{y}} \le 0\,, \tag{8}$$

where σ_{vM} represents the von Mises equivalent stress and σ_{y} is the yield stress.

In this study, the phenomenological Swift law is adopted to describe the hardening of the material. The isotropic work hardening function is given by:

$$\sigma_{\mathrm{y}} = K(\varepsilon_0 + \bar{\varepsilon}^{\mathrm{p}})^n\,, \tag{9}$$

where K, ε_0 and n are the material parameters, while $\bar{\varepsilon}^{\mathrm{p}}$ denotes the equivalent plastic strain. The initial yield stress is defined by $\sigma_0 = K(\varepsilon_0)^n$.

The total thermal strain is calculated as:

$$\boldsymbol{\varepsilon}^{\mathrm{th}} = \left(\alpha_T (T - T_{\mathrm{ref}}) - \alpha_{\mathrm{ini}} (T_{\mathrm{ini}} - T_{\mathrm{ref}})\right)\mathbf{I}\,, \tag{10}$$

where α_T and α_{ini} are the volumetric thermal expansion coefficients evaluated at the current temperature T and at the initial temperature T_{ini}, respectively. T_{ref} is the reference temperature used to define the thermal expansion coefficients and $\mathbf{I}$ denotes the second-order identity tensor.

3. Finite element model

The numerical simulations were carried out with the in-house finite element code DD3IMP, originally developed to simulate sheet metal forming processes [23]. The thermo-mechanical problem is solved using the staggered coupling algorithm proposed by Martins et al. [17], where the thermal and the mechanical problems are solved sequentially in each time increment.

The solution of the transient heat conduction problem is obtained by time integration using the Euler's backward method [24]. The evolution of the deformation is described by an updated Lagrangian scheme. In each increment, an explicit approach is used to calculate a trial solution for the deformation, which is iteratively corrected using a fully implicit Newton–Raphson scheme. Both the thermal and mechanical problems resort to the same finite element mesh (8-node hexahedral elements). However, full integration is adopted in the thermal problem, while the mechanical problem uses the selective reduced integration technique [25] to avoid volumetric locking.

3.1. SLM process conditions

In order to reduce the computational cost associated with the numerical simulation, the domain considered for the SLM process was significantly decreased. A single powder layer was studied considering a multi-track deposition. This single layer was scanned over solidified layers to enable thermo-mechanical conditions like the ones obtained in the SLM. The geometry of the initial domain is presented in Fig. 1. The substrate is a parallelepiped with 3 mm length, 1.5 mm width and 0.5 mm of thickness. The geometry of the solidified layers is defined also by a smaller parallelepiped, with the dimensions indicated in Fig. 1. The thickness of the powder layer is 40 μm in the region above the solidified layers [15]. All domain is composed by the same material: Ti-6Al-4V.

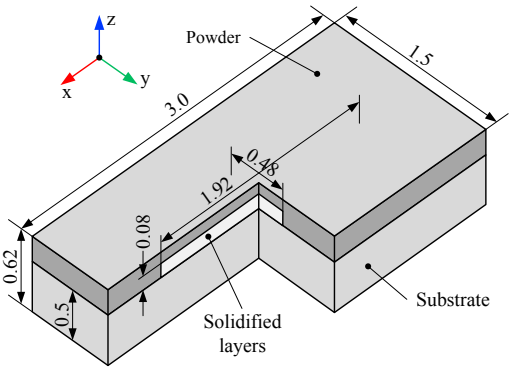

Fig. 1. Geometry of the initial solution domain (substrate, solidified layers and powder) used in the thermo-mechanical analysis of the SLM process. All dimensions in mm.

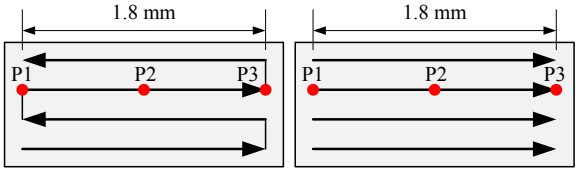

Fig. 2. Different laser scan strategies used in the simulation of a single layer multi-track SLM process. Identification of 3 points for temperature evaluation.

In order to assess the importance of the laser beam trajectory on the residual stresses, two scan strategies are adopted: (i) alternating and (ii) unidirectional, as shown in Fig. 2. The domain of the powder bed corresponding to the laser tracks presents a uniform finite element mesh with 10 μm of edge size. The set of process parameters considered in the numerical simulations of the SLM process are listed in Table 1. Taking into account the scanning speed considered, the processing time of each track is 3 ms.

Table 1. Process parameters used in the simulations of the SLM process.

Process parameter	Value	Reference
Laser power [W]	83	[15]
Laser absorptivity	0.35	[26]
Laser spot radius [μm]	50	
Scanning speed [mm/s]	600	[27]
Layer thickness [μm]	40	[15]
Hatching distance [μm]	120	
Preheating temperature [ºC]	200	[15]

3.2. Thermo-physical material properties

Since the SLM process initially comprises the material phase transformation from powder to liquid, which then cools down to solidification, three material phases were considered in the simulation: powder, solid and liquid. The powder material switches to liquid when the temperature rises to the melting point (1650ºC) and the liquid material solidifies when the temperature cools down to the melting point (bidirectional transformation). Moreover, each material phase requires a set of temperature dependent material properties [15], particularly those with a more pronounced variation in this temperature range. Also, the allotropic transformation occurring in the Ti-6Al-4V at elevated temperatures is neglected in the model, which simplifies the thermo-mechanical analysis of the solid phase material.

All thermal and physical properties of the liquid phase are assumed constant in the numerical simulation (see Table 2). In order to account for the convective heat transfer within the melt pool, the thermal conductivity coefficient is artificially increased. On the other hand, the mechanical strength of the liquid phase is very weak while the thermal expansion is neglected. The mass density of the powder and solid are assumed constant, as listed in Table 2. Note that the mass density of the powder phase is 60% of the solid Ti-6Al-4V, due to the assumption of 0.6 for the packing factor of the powder bed [21]. The mechanical strength of the powder phase is identical to the one considered for the liquid, but the thermal expansion coefficient is assumed 10% of the one adopted for the solid material.

Table 2. Temperature independent material properties for Ti-6Al-4V.

Property	Powder	Solid	Liquid
ρ [kg/m^3]	2600	4300	4300
c_p [J/kg·K]	-	-	820
k [W/m·K]	-	-	42
α [$\times 10^{-6}$ 1/K]	1.2	12.0	0.0
E [GPa]	0.05	-	0.05
ν [-]	0.34	0.34	0.34
σ_0 [MPa]	1.5	-	1.5
K [MPa]	10	-	10
n [-]	0.35	0.35	0.35

Table 3. Temperature dependent material properties for powder Ti-6Al-4V.

T [ºC]	c_p [J/kg·K]	k [W/m·K]
200	505	0.104
500	473	0.078
800	507	0.279
1000	610	0.813
1300	951	1.27
1650	1000	1.80

The temperature dependent material properties of the powder Ti-6Al-4V are listed in Table 3, namely the specific heat and the thermal conductivity coefficient. Note that the adopted thermal conductivity for the metallic powders is roughly 10 times smaller than that of the same bulk material due to the porosity in the powder bed [28].

Regarding the mechanical behavior, only the solid Ti-6Al-4V material presents a significant strength, which depends on the temperature. Both the initial yield stress and the Young modulus increase with the temperature, as shown in Table 4. The hardening coefficient of the Swift law is assumed constant with the temperature and it is identical for all material phases (see Table 2). Concerning the thermal properties, the specific heat increases slightly with the temperature, while the thermal conductivity coefficient ranges from about 9 W/(m·K) up to 27 W/(m·K). The presented temperature dependent thermophysical properties include the effect of the allotropic transformation. Nevertheless, the strains induced by this transformation were not included in the finite element model (see Eq. (5)).

Table 4. Temperature dependent material properties for solid Ti-6Al-4V.

T [ºC]	c_p [J/kg·K]	k [W/m·K]	E [GPa]	σ_0 [MPa]	K [MPa]
200	566	9.3	100	630	1500
650	646	15.3	55	300	770
761	665	17.0	20	110	350
872	685	18.5	10	55	120
1094	760	24.0	3	17	60
1650	820	27.0	0.05	1.5	10

4. Results and discussion

Since the residual stresses in the finished part are a consequence of the non-uniform material thermal expansion/contraction, an accurate solution for the thermal fields is vital. Thus, the temperature field and the thermal history are first presented and discussed. Then, the mechanical response is analyzed, namely the effect of the scan strategy on the generated residual stresses.

4.1. Temperature field

Adopting the alternating scan strategy (Fig. 2), the predicted temperature field on the top surface is presented in Fig. 3 for 7.9 ms of processing time (laser beam over P2). The geometry of the melt pool is approximately semielliptical, presenting 0.318 mm of length, 0.129 mm of width and 0.059 mm of depth. Since the thermal conductivity coefficient of the powder material is significantly lower than the value of the solid material (see Table 3 and 4), the resulting temperature distribution around the melt pool is asymmetric, as shown in Fig. 3.

The assignment of the material phase status is defined through the thermal history of each finite element, using the melting temperature as bound. Accordingly, the assigned material phase (powder, solid and liquid) is presented in Fig. 4 for 7.9 ms of processing time (alternating scan strategy). The material status is updated at the beginning of each time increment, defining the thermo-mechanical proprieties adopted in that increment.

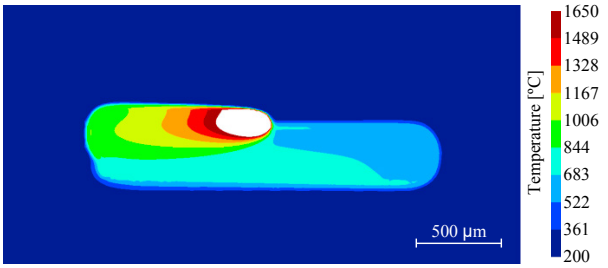

Fig. 3. Temperature distribution (top view) for 7.9 ms of processing time (laser beam over P2), considering the alternating scan strategy.

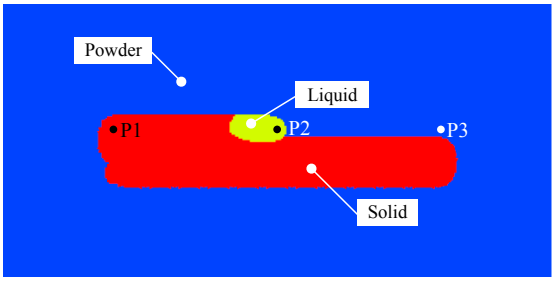

Fig. 4. Assigned material phase (powder, solid and liquid) for 7.9 ms of processing time (laser beam over P2), considering the alternating scan strategy.

The temperature history evaluated in 3 different points (Fig. 2) is presented in Fig. 5, comparing the two scanning strategies. The predicted temperature evolution in P2 is independent of the selected scan strategy. Considering the alternating scan strategy, the cooling down rate is identical in all points. On the other hand, the use of the unidirectional scan strategy leads to a larger cooling down rate at the end of the scan vector (see Fig. 2) than the alternating one.

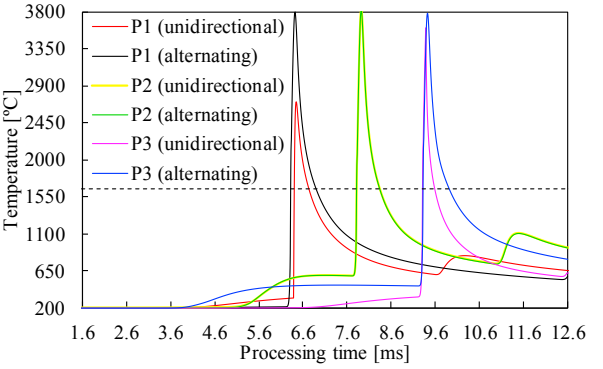

Fig. 5. Temperature history evaluated in 3 different points (see Fig. 2), comparing the two scanning strategies.

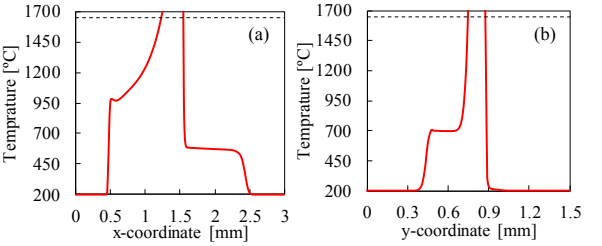

Fig. 6. Temperature profile evaluated in two lines on the top surface for 7.9 ms of processing time, considering the alternating scan strategy: (a) line connecting P1 and P3; (b) orthogonal line crossing P2.

The temperature distribution predicted on the top surface along two orthogonal directions crossing P2 is presented in Fig. 6 for 7.9 ms of processing time, considering the alternating scan strategy. The peak temperature (around 3800ºC) is a singularity inside the melt pool region. Its position is slightly behind the laser beam due to the movement of the heat source. Since the scanning speed is very high in comparison with the track length (Fig. 2) and the powder material presents a low value of thermal conductivity coefficient (Table 3), the cooling down is very slow outside the melt pool.

4.2. Residual stress

The predicted distribution for the von Mises equivalent stress in the built component is presented in Fig. 7, after 0.5 seconds of cooling time, comparing the two scanning strategies. Since the heat conduction is the dominant way of the heat diffusion, after 0.5 seconds of cooling down the temperature is approximately constant in all domain (290ºC). In fact, the printed layer cools down while both the substrate and the remaining powder warm up.

The adopted process parameters (see Table 1) lead to an overlap of the adjacent tracks. Thus, solidified material can be re-melted and posteriorly come back to solid. Accordingly, the

accumulated plastic strain of the solid must be withdrawn when the material goes back to the liquid phase. However, the developed mechanical model did not take into account this particular feature. Therefore, the predicted plastic strain is overestimated in the overlapped zone of adjacent tracks. This corresponds to an increase of the von Mises equivalent stress in overlap zones, due to the artificial increase of the flow stress, as shown in Fig. 7.

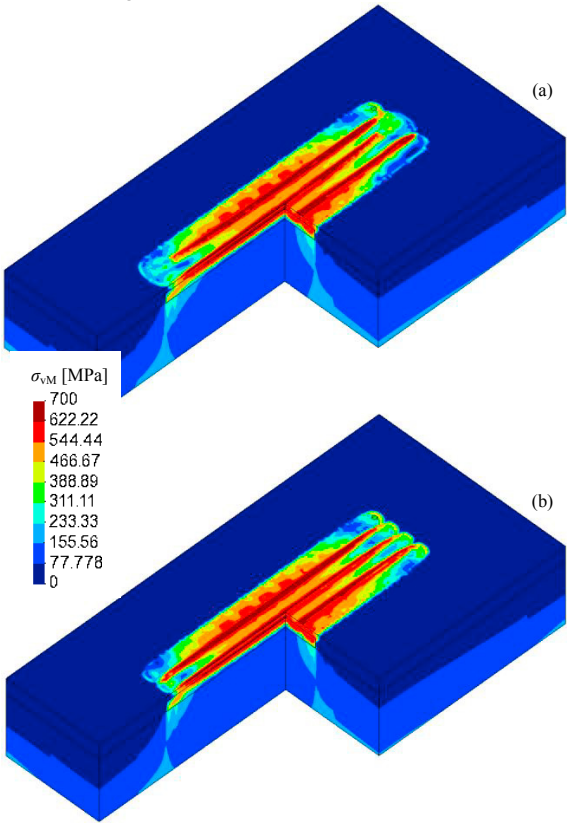

Fig. 7. Distribution of the von Mises equivalent stress in the built component after 0.5 seconds of cooling time, considering: (a) the alternating scan strategy; (b) the unidirectional scan strategy.

The predicted stress in the powder material is negligible due to the weak mechanical strength (see Table 2). In contrast, the higher stress values occur in the printed layer and in the solidified layers (solid material). This is a consequence of the value used for the volumetric thermal expansion coefficient of the solid material, which is higher than for other material phases (see Table 2). The impact of the laser scan strategy on the stress distribution is negligible, particularly at the mid-length of the scan vectors, which is in accordance with the predicted temperature history see (Fig. 5). However, the von Mises equivalent stress at the end of the scan vector is influenced by the laser scan strategy.

The largest stress component arises in the direction parallel to the scanning direction, which is in agreement with experimental studies [29]. The contour of the predicted longitudinal residual stress component is presented in Fig. 8, for the transverse cross-section corresponding to the half-length and adopting the alternating scan strategy. Due to the numerical problem related to the overlapping neighboring scan tracks, the adopted range for the stress values was reduced. Comparing the stress field before and after 0.5 seconds of cooling time, the longitudinal residual stress component increases considerably due to the temperature decrease, as shown in Fig. 8. In fact, the residual stresses are clearly positive (tension) in the solidified layers, presenting its maximum value in the interface between the printed layer and the solidified layers.

Adopting the unidirectional scan strategy, the contour of the predicted longitudinal residual stress component is presented in Fig. 9, for the transverse cross-section corresponding to the half-length. Since the predicted temperature history (Fig. 5) and the von Mises equivalent stress is identical for the alternating and unidirectional scan strategies, the impact of the laser scan strategy on the residual stress field is negligible (compare Fig. 8 with Fig. 9). Indeed, regarding this cross-section of the built component, the final location of the solid material is independent of the laser scan strategy, as shown in Fig. 8 (a) and Fig. 9 (a).

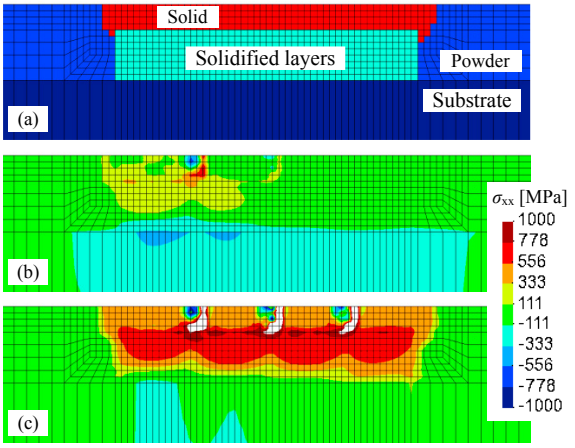

Fig. 8. Cross-section (half-length) of the component built with the alternating scan strategy: (a) assigned material phase; (b) contour of the longitudinal residual stress component before cooling; (c) contour of the longitudinal residual stress component after 0.5 seconds of cooling time.

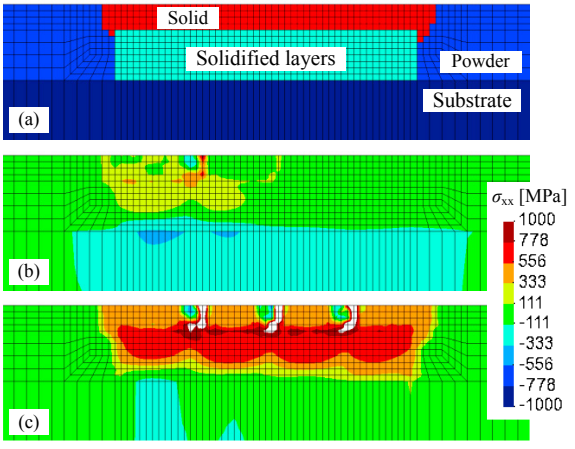

Fig. 9. Cross section (half-length) of the component built with the unidirectional scan strategy: (a) assigned material phase; (b) contour of the longitudinal residual stress component before cooling; (c) contour of the longitudinal residual stress component after 0.5 seconds of cooling time.

5. Conclusions

The thermo-mechanical model developed to simulate the SLM process is described in this study. This model comprises the transient thermal behavior, which is important to accurately predict the final residual stresses using the mechanical model. The influence of two different scan strategies on the residual stress is assessed by numerical simulation. The results show a strong coupling between the transient temperature history and the mechanical response. The shape and dimensions of the melt pool can be estimated based on the predicted temperature distribution, which is mainly dictated by the heat conduction mechanism.

Although the allotropic transformation was neglected, the generated residual stresses in the finished part are mainly a result of the non-uniform material thermal expansion/contraction. Higher temperature gradients developed higher residual stress. Indeed, the SLM process generates a non-uniform anisotropic stress field, with the largest component in the direction parallel to the scanning one. The residual stresses are positive (tension) in the solidified layers, presenting its maximum value in the interface with the current the printed layer. However, the differences between the two scan strategies in the von Mises equivalent stress are negligible, particularly at the mid-length of the scan vectors.

Acknowledgements

This research work was sponsored by national funds from the Portuguese Foundation for Science and Technology (FCT) under the project with reference PTDC/EME-EME/31657/2017 and by European Regional Development Fund (ERDF) through the Portugal 2020 program and the Centro 2020 Regional Operational Programme (CENTRO-01-0145-FEDER-031657) under the project MATIS (CENTRO-01-0145-FEDER-000014) and UID/EMS/00285/2020. The work forms part of the INTEGRADDE project, funded by the European Union's Horizon 2020 research and innovation progamme under Grant Agreement No. 820776.

References

[1] Khairallah SA, Anderson AT, Rubenchik A, King WE. Laser powder-bed fusion additive manufacturing: Physics of complex melt flow and formation mechanisms of pores, spatter, and denudation zones. Acta Mater 2016; 108:36–45.

[2] Sames WJ, List FA, Pannala S, Dehoff RR, Babu SS. The metallurgy and processing science of metal additive manufacturing. Int Mater Rev 2016; 61:315–360.

[3] Tan C, Zhou K, Ma W, Attard B, Zhang P, Kuang T. Selective laser melting of high-performance pure tungsten: parameter design, densification behavior and mechanical properties. Sci Technol Adv Mater 2018; 19:370–380.

[4] Mukherjee T, Zhang W, DebRoy T. An improved prediction of residual stresses and distortion in additive manufacturing. Comput Mater Sci 2017; 126:360–372.

[5] Das S. Physical Aspects of Process Control in Selective Laser Sintering of Metals. Adv Eng Mater 2003; 5:701–711.

[6] Ali H, Ghadbeigi H, Mumtaz K. Effect of scanning strategies on residual stress and mechanical properties of Selective Laser Melted Ti6Al4V. Mater Sci Eng A 2018; 712:175–187.

[7] Simonelli M, Tse YY, Tuck C. On the texture formation of selective laser melted Ti-6Al-4V. Metall Mater Trans A Phys Metall Mater Sci 2014; 45:2863–2872.

[8] Riedlbauer D, Scharowsky T, Singer RF, Steinmann P, Körner C, Mergheim J. Macroscopic simulation and experimental measurement of melt pool characteristics in selective electron beam melting of Ti-6Al-4V. Int J Adv Manuf Technol 2017; 88:1309–1317.

[9] Panwisawas C, Qiu C, Anderson MJ, Sovani Y, Turner RP, Attallah MM, Brooks JW, Basoalto HC. Mesoscale modelling of selective laser melting: Thermal fluid dynamics and microstructural evolution. Comput Mater Sci 2017; 126:479–490.

[10] Li C, Fu CH, Guo YB, Fang FZ. A multiscale modeling approach for fast prediction of part distortion in selective laser melting. J Mater Process Technol 2016; 229:703–712.

[11] Manvatkar V, De A, DebRoy T. Spatial variation of melt pool geometry, peak temperature and solidification parameters during laser assisted additive manufacturing process. Mater Sci Technol (United Kingdom) 2015; 31:924–930.

[12] Heeling T, Cloots M, Wegener K. Melt pool simulation for the evaluation of process parameters in selective laser melting. Addit Manuf 2017; 14:116–125.

[13] Markl M, Körner C. Multiscale Modeling of Powder Bed–Based Additive Manufacturing. Annu Rev Mater Res 2016; 46:93–123.

[14] Gibson I, Rosen D, Stucker B. Additive manufacturing technologies: 3D printing, rapid prototyping, and direct digital manufacturing, second edition. 2015.

[15] Parry L, Ashcroft IA, Wildman RD. Understanding the effect of laser scan strategy on residual stress in selective laser melting through thermo-mechanical simulation. Addit Manuf 2016; 12:1–15.

[16] Hussein A, Hao L, Yan C, Everson R. Finite element simulation of the temperature and stress fields in single layers built without-support in selective laser melting. Mater Des 2013; 52:638–647.

[17] Martins JMP, Neto DM, Alves JL, Oliveira MC, Laurent H, Andrade-Campos A, Menezes LF. A new staggered algorithm for thermomechanical coupled problems. Int J Solids Struct 2017; 122–123:42–58.

[18] Tran H-S, Tchuindjang JT, Paydas H, Mertens A, Jardin RT, Duchêne L, Carrus R, Lecomte-Beckers J, Habraken AM. 3D thermal finite element analysis of laser cladding processed Ti-6Al-4V part with microstructural correlations. Mater Des 2017; 128:130–142.

[19] Li JF, Li L, Stott FH. Comparison of volumetric and surface heating sources in the modeling of laser melting of ceramic materials. Int J Heat Mass Transf 2004; 47:1159–1174.

[20] Goldak J, Chakravarti A, Bibby M. A new finite element model for welding heat sources. Metall Trans B 1984; 15:299–305.

[21] Zhang Z, Huang Y, Rani Kasinathan A, Imani Shahabad S, Ali U, Mahmoodkhani Y, Toyserkani E. 3-Dimensional heat transfer modeling for laser powder-bed fusion additive manufacturing with volumetric heat sources based on varied thermal conductivity and absorptivity. Opt Laser Technol 2019; 109:297–312.

[22] Yang YP, Jamshidinia M, Boulware P, Kelly SM. Prediction of microstructure, residual stress, and deformation in laser powder bed fusion process. Comput Mech 2018; 61:599–615.

[23] Menezes LF, Teodosiu C. Three-dimensional numerical simulation of the deep-drawing process using solid finite elements. J Mater Process Technol 2000; 97:100–106.

[24] Martins JMP, Alves JL, Neto DM, Oliveira MC, Menezes LF.

Numerical analysis of different heating systems for warm sheet metal forming. Int J Adv Manuf Technol 2016; 83:897–909.

[25] Hughes TJR. Generalization of selective integration procedures to anisotropic and nonlinear media. Int J Numer Methods Eng 1980; 15:1413–1418.

[26] Fischer P, Romano V, Weber HP, Karapatis NP, Boillat E, Glardon R. Sintering of commercially pure titanium powder with a Nd:YAG laser source. Acta Mater 2003; 51:1651–1662.

[27] Ganeriwala RK, Strantza M, King WE, Clausen B, Phan TQ, Levine LE, Brown DW, Hodge NE. Evaluation of a thermomechanical model for prediction of residual stress during laser powder bed fusion of Ti-6Al-4V. Addit Manuf 2019; 27:489–502.

[28] Moser D, Pannala S, Murthy J. Computation of Effective Thermal Conductivity of Powders for Selective Laser Sintering Simulations. J Heat Transfer 2016; 138.

[29] Robinson J, Ashton I, Fox P, Jones E, Sutcliffe C. Determination of the effect of scan strategy on residual stress in laser powder bed fusion additive manufacturing. Addit Manuf 2018; 23:13–24.